STM JOURNALS

Journal of
Thin Films, Coating Science
Technology and Application

ISSN: 2455-3344
Volume 12, Issue 3, 2025
September–December
DOI (Journal): 10.37591/JoTCSTA

https://journals.stmjournals.com/jotcsta

Research JoTCSTA

Kinetics of Crystallization and Microstructural Evolution of Commercial Fluorophlogopite Machinable Glass-Ceramics in the System $SrO{\cdot}4MgO{\cdot}Al_2O_3{\cdot}6SiO_2{\cdot}2MgF_2$ with Varying in B_2O_3

Priyabrata Manna[1,*], Chandan Santra[1], Tapas Kumar Ghosh[2], P.K. Maiti[3], Totan Ghosh[4,*]

Abstract

Glass materials based on fluorophlogopite stoichiometry with varying concentrations of B_2O_3 were synthesized using the melt-casting method, followed by heat treatment at different crystallization temperatures. The resulting glass and glass–ceramic samples were characterized using differential thermal analysis (DTA), scanning electron microscopy (SEM), X-ray diffraction (XRD), and Fourier-transform infrared (FT-IR) spectroscopy. Kinetic analysis revealed that the activation energies required for the formation of glass–ceramics were 192.77 kJ mol^{-1} and 210.47 kJ mol^{-1}, as calculated by the Kissinger and Ozawa methods, respectively. XRD analysis indicated the formation of strontium fluorophlogopite and strontium aluminum silicate as the predominant crystalline phases at elevated heat treatment temperatures. These phases exhibited high aspect ratios and an interlocking microstructure, as confirmed by SEM observations. FT-IR spectra of the glass samples with higher B_2O_3 content revealed the coexistence of B–O bonds in both BO_4 tetrahedral and BO_3 trigonal coordination, along with AlO_4 and SiO_4 tetrahedral units forming the glass network structure. The combined analysis of thermal, structural, and spectroscopic data highlights the influence of B_2O_3 concentration and heat-treatment parameters on the microstructural evolution and crystallization kinetics of fluorophlogopite-based glass–ceramics. This study demonstrates that optimizing the B_2O_3 content and controlled heat treatment enables the formation of interlocked crystalline phases with enhanced mechanical stability, offering potential for high-temperature and dielectric applications in advanced material systems.

***Author for Correspondence**
Priyabrata Manna
E-mail: totan.chem@gmail.com

1Assistant Professor, Department of Chemistry, Brainware University, 398, Ramkrishnapur Road, Barasat, Kolkata, West Bengal, India
2Assistant Professor, Department of General Science & Huminities Calcutta Institute of Technology, Uluberia-Howrah, West Bengal, India
[3]Associate Professor, Ceramic Engineering Division, Department of Chemical Technology, University of Calcutta, 92 A. P. C. Road, Kolkata, West Bengal, India
[4]Assistant Professor, Department of Applied Chemistry, Maulana Abul Kalam Azad University of Technology, Simhat, Haringhata, West Bengal, India

Received Date: July 08, 2025
Accepted Date: July 17, 2025
Published Date: September 17, 2025

Citation: Priyabrata Manna, Chandan Santra, Tapas Kumar Ghosh, P.K. Maiti, Totan Ghosh. Kinetics of Crystallization and Microstructural Evolution of Commercial Fluorophlogopite Machinable Glass-Ceramics in the System $SrO{\cdot}4MgO{\cdot}Al_2O_3{\cdot}6SiO_2{\cdot}2MgF_2$ with Varying in B_2O_3. Journal of Thin Films, Coating Science Technology and Application. 2025; 12(3): 1–16p.

Keywords: Glass-ceramics, powder XRD, SEM, crystallization temperature, microstructure

INTRODUCTION

Glass-ceramics based on fluorophlogopite stoichiometry are typically two-dimensional mica crystalline materials that originate from fluorine-containing vitreous matrices through controlled nucleation and crystallization of highly viscous glass-forming melts [1–5]. The transition from the amorphous glass to crystalline state in these materials occurs via two distinct stages: nucleation (an endothermic process), followed by crystal growth (an exothermic process) [6]. One of the most distinctive characteristics of mica-based

glass-ceramics is their exceptional machinability. This is attributed to their blocky mica sheet structures, which inhibit crack propagation through the bulk and instead promote cleavage along mica's intrinsic crystal-glass or crystal-crystal interfaces. The resulting crack deflection, branching, and blunting mechanisms contribute significantly to their ease of machining [7].

In particular, phlogopite-type mica glass-ceramics exhibit superior machinability due to the layered lattice structure of sheet silicates, which assemble into a 'house-of-cards' microstructure. This architecture facilitates perfect basal cleavage along the (001) planes of mica crystals. In addition to machinability, these materials demonstrate excellent mechanical performance, including high flexural strength, enhanced fracture toughness, thermal shock resistance, and favorable dielectric properties.

Beall was among the first to explore alkaline-earth-containing fluormica glass–ceramics [8]. Subsequently, Hoda and Beall examined a series of compositions incorporating alkaline earth elements such as barium, calcium, and strontium, based on fluorophlogopite stoichiometry [7]. These glass compositions exhibited a strong tendency to crystallize spontaneously during casting. The resulting glass-ceramics demonstrated notable properties, including high mechanical strength and excellent thermal stability. Notably, strontium-containing variants displayed an unusual behavior of water-induced swelling and spontaneous disintegration into clay-like particles, highlighting their unique physicochemical characteristics.

Greene *et al.* systematically altered a K_2O–BaO–MgO–SiO_2–B_2O_3–MgF_2 fluormica glass composition by replacing BaO, B_2O_3, and MgF_2 with K_2O, Al_2O_3, and MgO, respectively [9]. Potassium substitution for barium led to larger molar volumes and higher coefficients of thermal expansion, accompanied by lower fractional glass compactness, reduced micro-hardness, and a depression of the glass-transition temperature.

James *et al.* investigated calcium-containing phosphate glasses within the (100−X)CaO–P_2O_5–X B_2O_3 compositional system [10–14]. Their findings demonstrated that the incorporation of B_2O_3 significantly enhanced bulk (volume) nucleation within the glass matrix. Notably, bulk crystallization was prominent when the B_2O_3 content ranged between 15 and 25 mol%, whereas compositions outside this range predominantly exhibited surface crystallization behavior.

Honda *et al.* identified a novel fluorophlogopite phase within a machinable glass-ceramic system composed of SiO_2–Al_2O_3–MgO–Na_2O/K_2O–F^- [12]. This newly formed mica exhibited machinability that was 4 to 5 times greater than that of conventional "house-of-cards" structured phlogopite-based glass-ceramics. Their study also revealed that phase separation occurred in the parent glass during the nucleation and crystallization stages under controlled heat treatment, which played a crucial role in the development of the enhanced microstructure.

Henry *et al*. investigated the nucleation and crystallization behavior of glass-ceramics within the 8SiO_2–YAl_2O_3–4MgO–2MgF_2–BaO system, where the alumina content (Y) was systematically varied between 1.5 and 3.0 mol.% [15]. Their results showed that decreasing the Al_2O_3 content led to a reduction in both the glass transition temperature and the onset of crystallization, while simultaneously enhancing bulk crystallization. The initial crystallization peak was attributed to the formation of barium fluorophlogopite. In contrast, higher alumina concentrations favored the development of additional crystalline phases, including cordierite, mullite, and barium aluminium silicate.

Henry *et al.* examined the influence of varying Al_2O_3 content (Y=1.5–3.0 mol%) in the 8SiO_2–YAl_2O_3–4MgO–2MgF_2–BaO glass-ceramic system on microstructure, hardness, and machinability [16]. Their findings indicated that both mechanical hardness and machinability were strongly governed by the development of an interconnected "house-of-cards" microstructure, characteristic of layered mica crystals. This structural arrangement played a critical role in enhancing the material's workability and mechanical response.

Uno *et al*. recently reported on glass-ceramics derived from a ternary system comprising $Ca_3(PO_4)_2$, $Ba_{0.5}\cdot Mg_3(AlSi_3O_{10})F_2$, and $Mg_2\cdot Al_4\cdot Si_5\cdot O_{18}$ [17–19]. Although detailed compositional data were not fully disclosed, the formulations were noted to be close to the $Ba_{0.5}\cdot Mg_3(AlSi_3O_{10})\ F_2$ stoichiometry. The resulting glass-ceramics demonstrated significantly enhanced mechanical performance, exhibiting flexural strengths of up to 500 MPa and fracture toughness values around 3.2 $MPa.m^{1/2}$. These properties were reported to surpass those of conventional mica-based glass-ceramics by a factor of two to three, highlighting the potential of barium-containing systems for high-performance applications.

In our earlier study by Mallik *et al*. [13], we investigated the crystallization behavior and microstructural evolution of mica phases in strontium fluorophlogopite-based glass-ceramics, derived from the $BaO\cdot 4MgO\cdot Al_2O_3\cdot 6SiO_2\cdot 2MgF_2$ system [13]. The findings revealed predominantly homogeneous crystallization throughout the glass matrix, with fluorine playing a critical role in facilitating the onset of crystallization. The incorporation of B_2O_3 was also shown to influence the nucleation dynamics and overall microstructural development.

To the best of our knowledge, no prior study has systematically explored the effects of varying B_2O_3 content on nucleation behavior, crystallization kinetics, crystal growth, and microstructural evolution in strontium fluormica-based glass-ceramics.

The primary objective of this study is to elucidate the role of B_2O_3 in influencing glass nucleation, the crystallographic characteristics of precipitated mica phases, and the resulting microstructural morphology developed during controlled heat treatment in glass-ceramic materials based on the $SrO\cdot 4MgO\cdot Al_2O_3\cdot 6SiO_2\cdot 2MgF_2$ system.

EXPERIMENTAL WORK

Parent Glass Preparation

Glass batches were formulated using high-purity, analytical-grade reagents, including $SrCO_3$, SiO_2, MgO, Al_2O_3, MgF_2, and H_3BO_3, primarily sourced from E. Merck (Table 1). The base composition was derived from the general formula $SrO\cdot 4MgO\cdot Al_2O_3\cdot 6SiO_2\cdot 2MgF_2$, with B_2O_3 content systematically varied by incorporating 0, 4, and 6 wt% to investigate its influence on glass-ceramic development. Each batch was thoroughly homogenized through wet milling in an attrition mill before being melted in a platinum crucible at 1450 °C for 2 h in an electrically heated furnace. During melting, the batch was periodically stirred using a platinum rod to ensure compositional uniformity.

The molten glass was cast into a preheated cast-iron mold to form blocks measuring approximately 55 mm×30 mm×10 mm. Once sufficient mechanical strength had developed, the blocks were removed from the mold and transferred immediately to an annealing furnace at 650°C, where they were held for 1 h and subsequently cooled to room temperature at a natural rate. Post-annealing, the glass blocks were sectioned into 2–3 mm thick specimens using a precision low-speed diamond saw (Buehler). A portion of each sample was ground to a fine powder (~75 μm) for differential thermal analysis (DTA) to determine the glass transition temperature (Tg) and the crystallization onset/peak temperatures (Tp).

Heat Treatment

The glass samples were initially heated to the designated nucleation temperature at a controlled rate of 10°C/min and held isothermally for 2 h to facilitate the formation of nucleation centers (Table 1). Following this step, the samples were further heated to the respective crystallization temperature at a slower rate of 2°C/min and maintained at this temperature for 5 h to allow for adequate crystal growth and microstructural development.

Table 1. Chemical compositions of three glass batches in gm (weight%).

Batch no.	$SrCO_3$	MgO	SiO_2	Al_2O_3	MgF_2	H_3BO_3
B2	17.284	18.55	41.47	11.73	14.34	3.56
B4	16.94	18.17	40.63	11.49	14.04	7.12
B6	16.57	17.79	39.78	11.25	13.75	10.68

Characterization

Differential thermal analysis (DTA) was conducted using a Shimadzu DT40 thermal analyzer, with α-alumina powder employed as the reference material. The synthesized glass samples were initially crushed and ground to a fine powder (~75 μm) suitable for thermal analysis. Non-isothermal DTA measurements were carried out on ~17 mg of powdered glass, which had been previously crystallized at different temperatures. These experiments were performed at multiple heating rates of 5, 10, 15, and 20°C/min, over the temperature range from ambient to 1000°C, to investigate the crystallization behavior. Activation energy for the glass-to-crystal transformation was estimated for each glass composition using the Kissinger and Ozawa methods, providing insight into the crystallization kinetics.

Phase identification was performed using X-ray diffraction (XRD) analysis with a PANalytical X'Pert PRO diffractometer equipped with a Ni-filtered Cu $K\alpha_1$ radiation source (λ=1.5406 Å), operated at 40 kV and 30 mA. Scans were collected at a rate of 2° (2θ) per minute over a 2θ range of 10–70°. Crystalline phases were identified by comparison with standard reference data from the ICDD PDF-2 database (JCPDS numbers).

Microstructural characterization was carried out using scanning electron microscopy (SEM) in secondary electron imaging (SEI) mode with a ZEISS instrument operated at an accelerating voltage of 20 kV. Prior to imaging, all samples were mechanically polished using diamond paste and chemically etched with a dilute hydrofluoric acid (HF) solution to enhance surface contrast. Elemental composition of the crystalline phases was further examined using energy-dispersive X-ray spectroscopy (EDX).

Fourier transform infrared (FTIR) spectroscopy was employed to investigate the structural features of the glasses. The analyses were conducted using a PerkinElmer spectrometer (Spectrum V6.3.5) over the wavenumber range of 400–4000 cm^{-1}, with potassium bromide (KBr) as the background reference.

Bulk density measurements were performed using Archimedes' principle, based on water displacement, to assess the physical density of the glass and glass-ceramic specimens.

RESULTS AND DISCUSSION

Differential Thermal Analysis

The differential thermal analysis (DTA) profiles for the three glass compositions, recorded at heating rates of 5, 10, 15, and 20°C/min, are presented in Figures 1–3. Each composition exhibited a single prominent exothermic crystallization peak, indicating a dominant crystallization event. From the DTA curves, the glass transition temperature (Tg) and peak crystallization temperature (Tp) were extracted. Notably, the Tp was found to shift to higher temperatures with increasing B_2O_3 content, suggesting enhanced thermal stability of the glass structure. This trend is consistent with earlier findings by James *et al.* [10]. In contrast, the Tg remained nearly invariant across all compositions, indicating minimal influence of B_2O_3 on the onset of structural relaxation.

As the crystallization peak temperature increases while Tg remains relatively constant, the thermal stability parameter ($\Delta T = Tp - Tg$) correspondingly increases. A higher ΔT value is typically associated

with improved glass stability and resistance to devitrification. The observed increase in ΔT with higher B_2O_3 concentrations aligns with previous reports highlighting the stabilizing effect of network-forming oxides such as B_2O_3 in silicate glass systems.

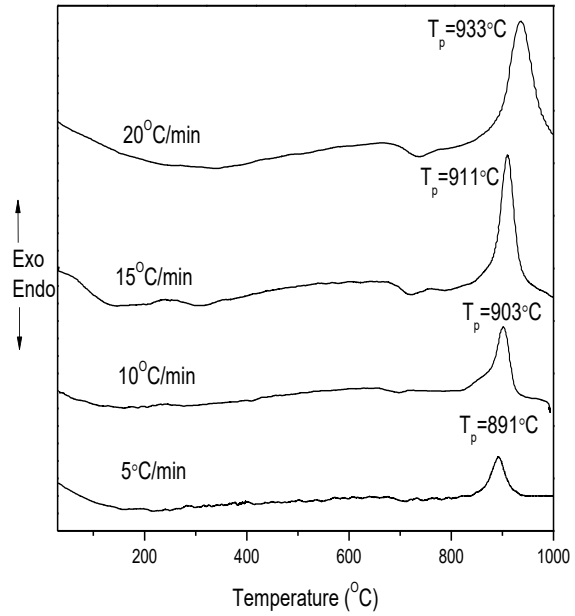

Figure 1. Differential thermal analysis plots of glass sample B2 of varying heating rate: (1) 5°C/min, (2) 10°C/min, (3) 15°C/min, (4) 20°C/min.

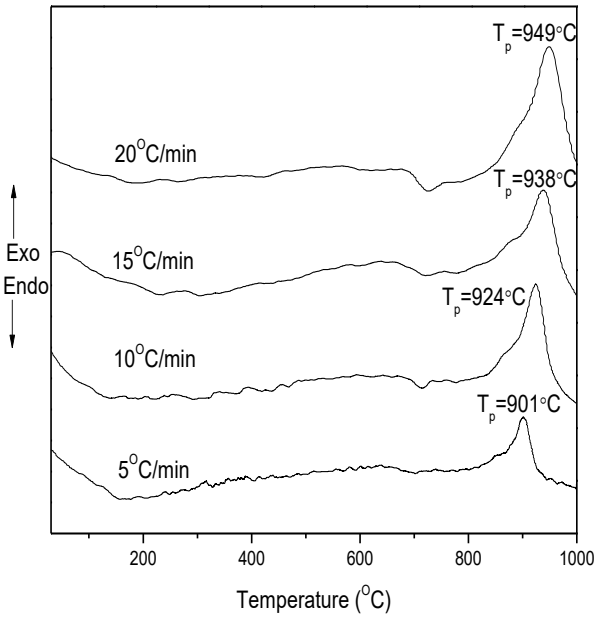

Figure 2. Differential thermal analysis plots of glass sample B4 of varying heating rate: (1) 5°C/min, (2) 10°C/min, (3) 15°C/min, (4) 20°C/min.

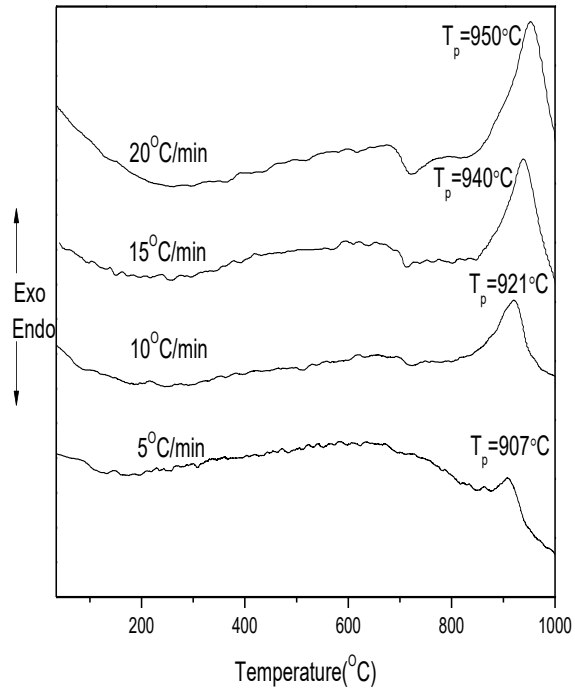

Figure 3. Differential thermal analysis plots of glass sample B6 of varying heating rate: (1) 5°C/min, (2) 10°C/min, (3) 15°C/min, (4) 20°C/min.

Kinetics of Crystallization Study

The crystallization kinetics of glass materials was analyzed using the Johnson–Mehl–Avrami (JMA) model [20–22], which describes the time-dependent crystallized volume fraction (X) during the transformation process.

The JMA equation is expressed as: $X=1-\exp\{-(kt)^n\}$ (1)

Here, X represents the fraction of crystallized material at a given time t, k is the reaction rate constant, and n is the Avrami exponent, a dimensionless parameter that reflects the mechanism of nucleation and the dimensionality of crystal growth.

For non-isothermal conditions, the JMA model can be adapted using the Kissinger and Ozawa methodologies to evaluate the activation energy (E) of crystallization processes [23–25].

The Kissinger equation is formulated as:
$\mathrm{Ln}\{T_p^2/\beta\}=E/RT_p+C$ (2)

and the Ozawa equation is:
$\mathrm{Ln}\beta=-E/RT_p+C$ (3)

In these equations, T_p is the temperature corresponding to the peak of the exothermic crystallization event observed in DTA curves, β is the applied heating rate, E denotes the activation energy for crystallization, R is the universal gas constant, and C is a constant related to the pre-exponential factor.

The activation energy (E) was determined by plotting experimental data obtained from non-isothermal DTA measurements at multiple heating rates (Figures 4–9). Linear fitting of the respective Kissinger and Ozawa plots allowed for accurate calculation of E, thereby providing insight into the crystallization kinetics of the glass samples under investigation (Table 2).

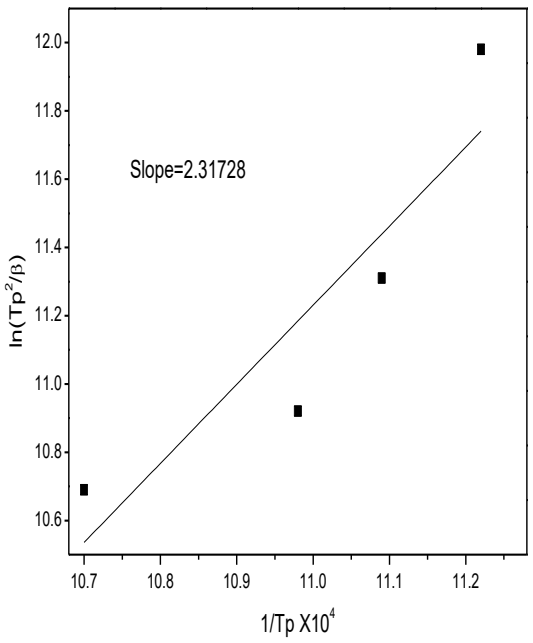

Figure 4. Kissinger plot of $\ln(T_p^2/\beta)$ against $1/T_p$ for the crystallization temperature of the B2 sample.

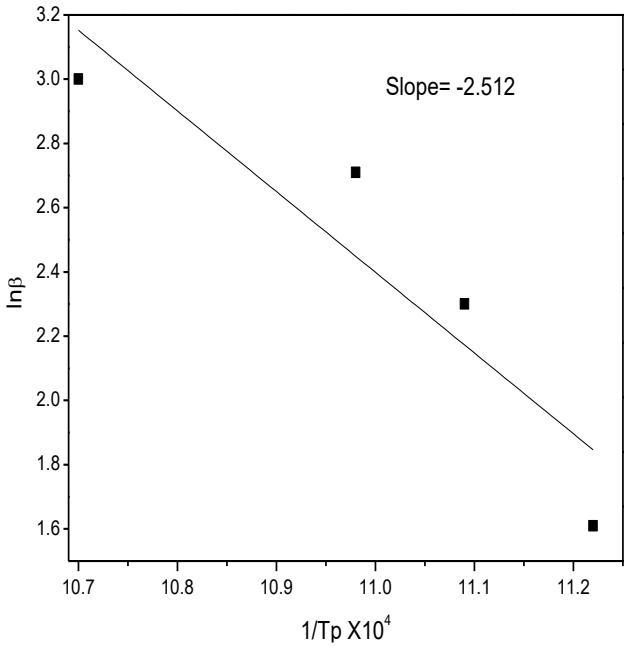

Figure 5. Ozawa plot of $\ln\beta$ against $1/T_p$ for the crystallization temperature of the B2 sample.

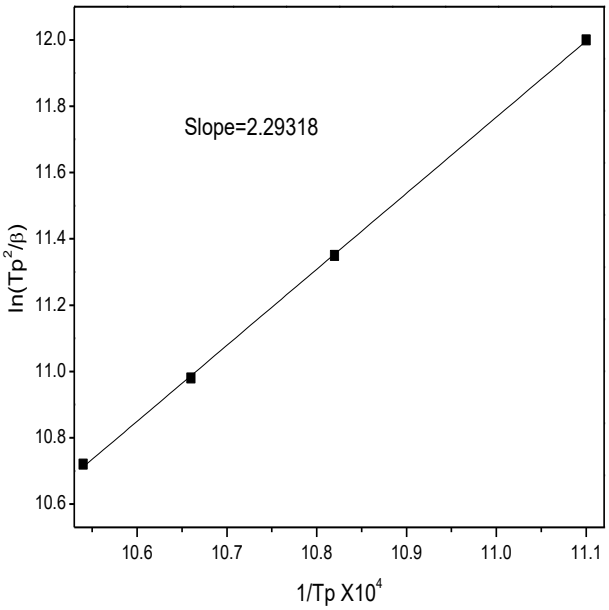

Figure 6. Kissinger plot of $\ln(T_p^2/\beta)$ against $1/T_p$ for the crystallization temperature of the B4 sample.

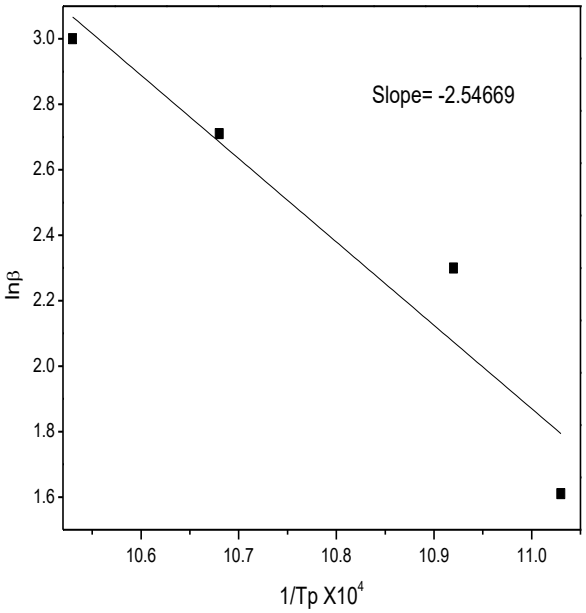

Figure 7. Ozawa plot of $\ln\beta$ against $1/T_p$ for the crystallization temperature of the B4 sample.

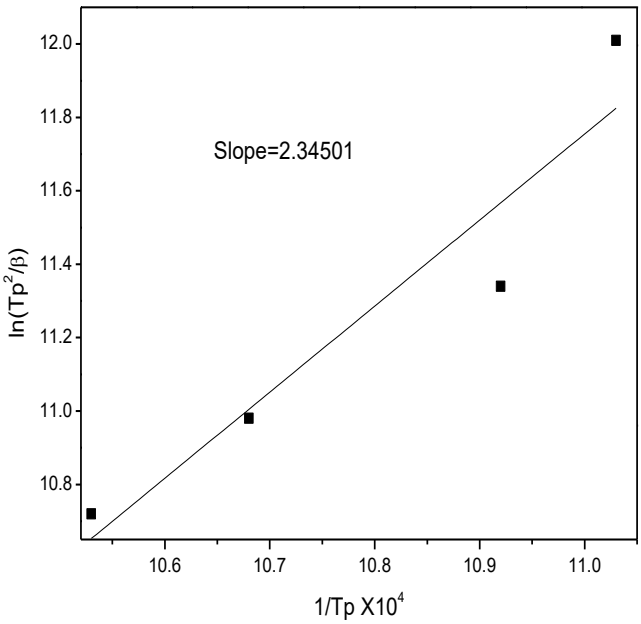

Figure 8. Kissinger plot of $\ln(T_p^2/\beta)$ against $1/T_p$ for the crystallization temperature of the B6 sample.

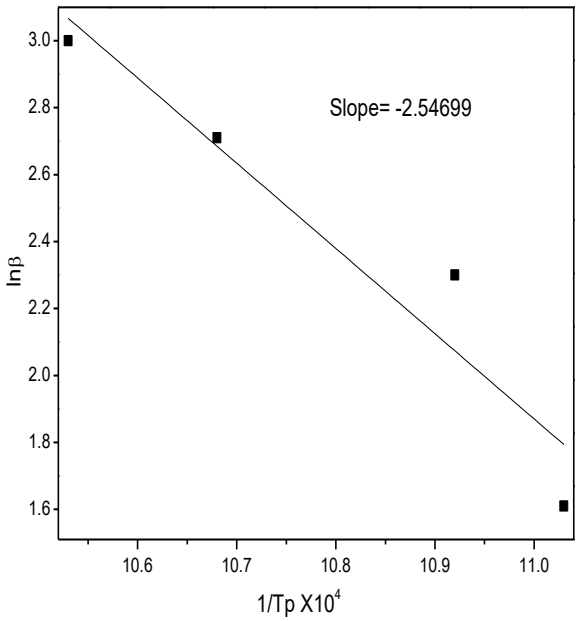

Figure 9. Ozawa plot of $\ln\beta$ against $1/T_p$ for the crystallization temperature of the B6 sample.

It was observed that the activation energy values obtained from both the Kissinger and Ozawa models are in good agreement. With increasing B_2O_3 content, the activation energy (E) associated with crystal growth, representing the energy barrier for transformation from the amorphous to the crystalline phase, also increases. Specifically, values derived from the Kissinger equation range from 192.66 to 194.96 kJ.mol^{-1}, while the Ozawa method yields a corresponding increase from 208.85 to 211.73 kJ.mol^{-1}. The average activation energies calculated across all samples were 192.76 and 210.47 kJ.mol^{-1} for the Kissinger and Ozawa methods, respectively.

Table 2. The value of Activation energy {Kissinger equation (E_K) and Ozawa equation (E_O)} and Avrami exponent [26, 27].

Batch name	Heating rate (°C/min)	Crystal peak temperature (T_P)	Average E_K (kJ/mol)	Average E_O (kJ/mol)	Avrami Exponent from Kissinger eq.	Avrami Exponent from Ozawa eq.
B2	5	1164	190.68	208.85	1.77	1.74
	10	1167			1.89	1.63
	15	1184			1.90	1.73
	20	1206			2.80	2.57
B4	5	1174	192.66	210.83	2.23	2.02
	10	1197			2.41	2.18
	15	1211			2.50	2.26
	20	1222			3.49	3.14
B6	5	1180	194.96	211.73	2.22	2.01
	10	1194			4.15	3.99
	15	1213			4.23	3.83
	20	1223			3.67	3.11

In terms of crystallization mechanism, the Avrami exponent (n) provides insight into the dimensionality of crystal growth. For sample B2, $n \approx 2$ suggests a two-dimensional growth process. However, with increased B_2O_3 content, samples B4 and B6 show higher n values of approximately 2.52 and 3.41, respectively, indicating a transition toward more complex growth behavior, spanning from two- to three-dimensional crystal formation. This evolution in n suggests a shift in the dominant crystallization mechanism from surface-driven nucleation to bulk crystallization, as B_2O_3 content increases [22–28].

$$n=2.5/\Delta T \times RT_p/E \quad (4)$$

X-Ray Diffraction

The identification of crystalline phases formed during heat treatment of the glass-ceramic samples was carried out using X-ray diffraction (XRD), with reference to standard JCPDS files listed in Tables 3–5. The XRD patterns of the three glass compositions, subjected to controlled heat treatments at 800, 900, 1000, and 1100°C for 5 h, are presented in Figures 10–12. The principal crystalline phases detected across the different compositions include strontium fluorophlogopite, strontium aluminium silicate, and cordierite.

At 800°C, no discernible crystalline phases were observed in any of the B2, B4, or B6 glass samples, suggesting insufficient thermal energy for nucleation and growth. Upon increasing the temperature to 900°C, strontium fluorophlogopite emerged as the dominant phase in all compositions, accompanied by minor peaks corresponding to strontium aluminium silicate, though the intensity varied among the samples.

With further heat treatment at 1000°C, strontium fluorophlogopite remained the major crystalline phase, and the intensity of strontium aluminium silicate peaks increased, indicating its continued growth. At 1100°C, both strontium fluorophlogopite and strontium aluminium silicate were observed as co-dominant phases. Additionally, minor peaks attributable to enstatite and cordierite were detected, particularly in the B4 and B6 samples, which contain higher B_2O_3 concentrations.

Notably, the relative intensity and abundance of strontium fluorophlogopite peaks increased progressively with heat treatment up to 1000°C across all compositions. This trend highlights the role of B_2O_3 in facilitating enhanced crystallization and phase development at elevated temperatures.

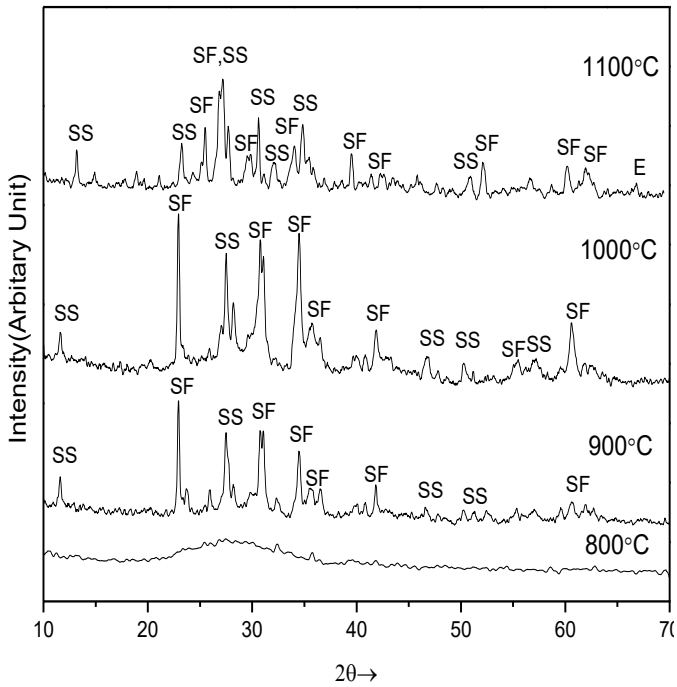

Figure 10. XRD patterns for B2 glass and glass-ceramics samples at different crystallization temperatures (800–1100°C).

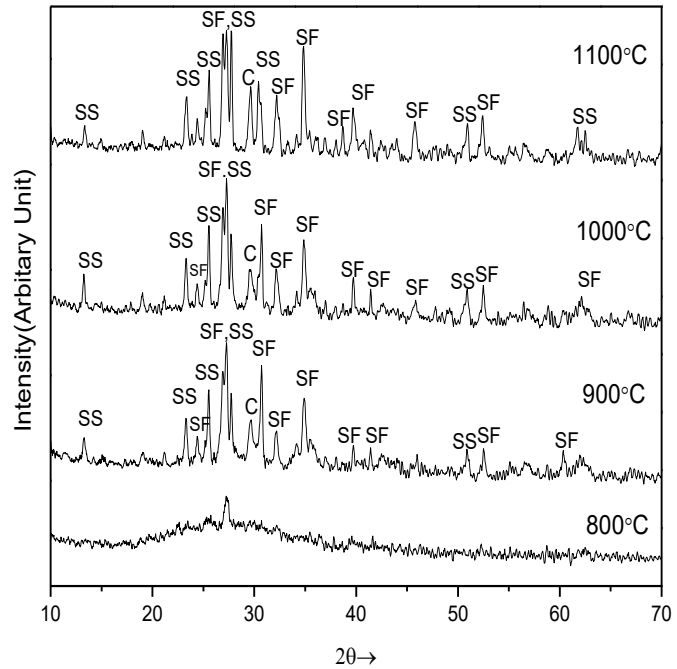

Figure 11. XRD patterns for B4 glass and glass-ceramics samples at different crystallization temperatures (800–1100°C).

Table 3. List of JCPDS files used to identify different crystal phases present in sample B2.

Batch no.	Crystal phase	Notation	JCPDS reference file
B2	Strontium fluorophlogopite	SF	00-019-0117
	Strontium aluminium silicate	SS	00-038-1454
	Enstatite	E	00-002-0546

Table 4. List of JCPDS files used to identify different crystal phases present in sample B4.

Batch no.	Crystal phase	Notation	JCPDS reference file
B4	Strontium fluorophlogopite	SF	00-019-0117
	Strontium aluminium silicate	SS	00-038-1454
	Cordierite	C	00-013-0294

Table 5. List of JCPDS files used to identify different crystal phases present in sample B6.

Batch no.	Crystal phase	Notation	JCPDS reference file
B6	Strontium fluorophlogopite	SF	00-019-0117
	Strontium aluminium silicate	SS	00-038-1454
	Cordierite	C	00-013-0294

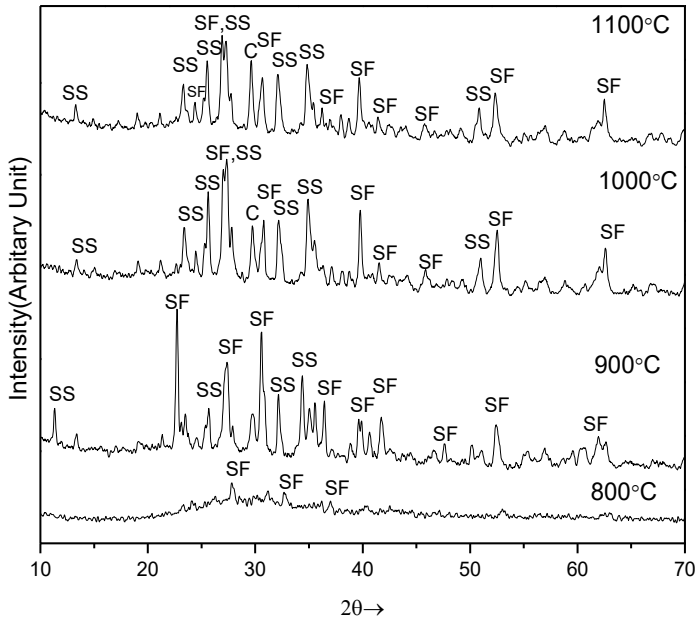

Figure 12. XRD patterns for B6 glass and glass-ceramics samples at different crystallization temperatures (800–1100°C).

Scanning Electron Microscope (SEM)

The microstructural evolution of the glass-ceramics following polishing and chemical etching is illustrated in Figures 13–15. At a treatment temperature of 800°C, no crystalline features were evident in any of the B2, B4, or B6 compositions, indicating the glassy nature of the material at this stage. Upon increasing the temperature to 900°C, submicron-sized blocky crystals began to emerge across all batches, signaling the onset of nucleation and initial crystal growth.

At 1000°C, the development of elongated, lath-like crystals with high aspect ratios was observed in all samples, accompanied by residual blocky morphologies. These lath-shaped crystals became more pronounced at 1100°C, where a well-developed interlocking microstructure was evident. Notably, the so-called "house of cards" microstructure, characteristic of fluorophlogopite crystallization, was observed at this temperature, as seen in Figures 13 and 14.

The B6 composition, which contains the highest concentration of B_2O_3, exhibited crystals with a particularly high aspect ratio and a blockier microstructure, as shown in Figure 15. This configuration

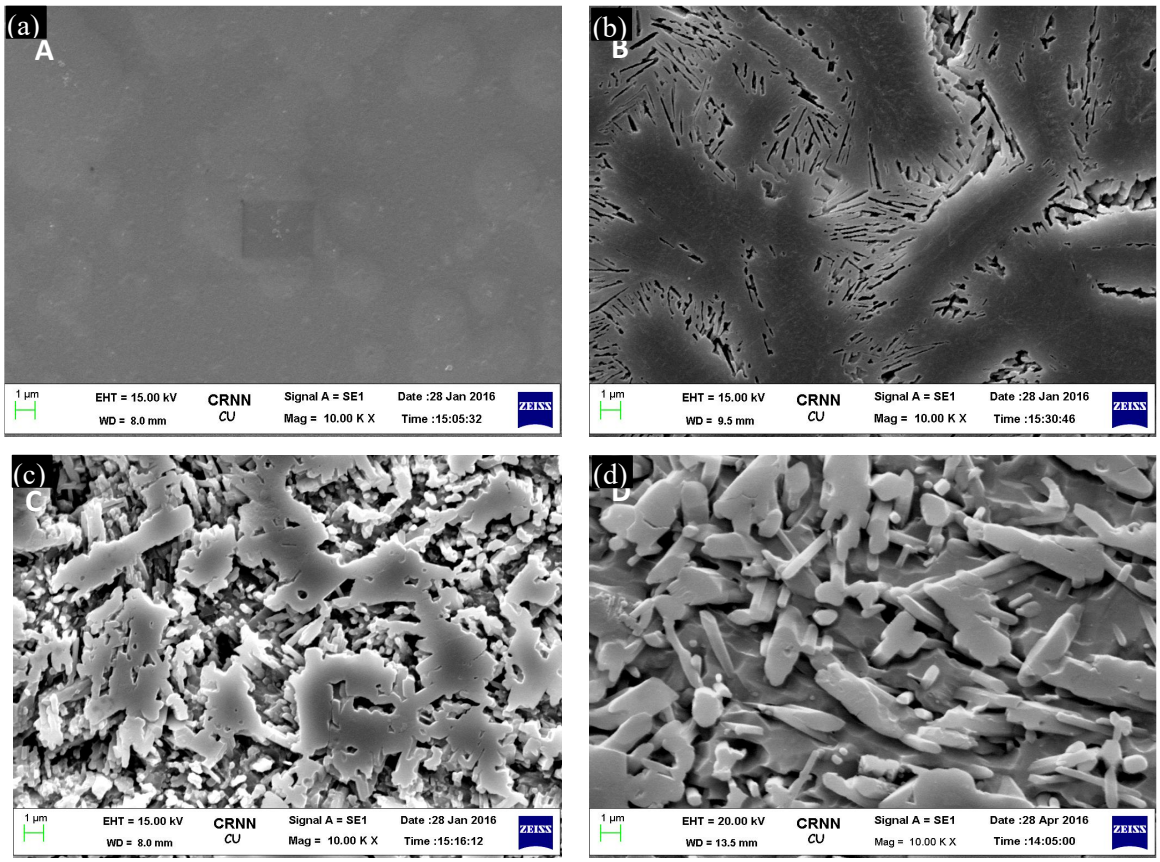

Figure 13. SEM photographs of the polished and etched surface of the glass-ceramics sample of B2 ceramized at (a) 800°C, (b) 900°C, (c) 1000°C, (d) 1100°C for 5 h.

may contribute to improved resistance to crack propagation due to the interruption of crack pathways by mica sheets.

Moreover, micrographs of B4 and B6 compositions revealed that crystallization initiated preferentially at the surface and progressively extended into the interior of the glass matrix. This transition resulted in the formation of three-dimensional, blocky, dendritic-shaped crystals, indicative of a shift from surface to bulk crystallization with increasing B_2O_3 content. These morphological changes underscore the significant influence of B_2O_3 on the nucleation behavior and microstructural evolution in strontium fluoromica-based glass-ceramics.

EDX analysis

The elemental composition of the crystalline phases formed at 1100°C was analyzed using Energy Dispersive X-ray (EDX) spectroscopy, as shown in Figure 16. The EDX spectra confirmed the presence of key elements, including oxygen, fluorine, magnesium, aluminium, silicon, and strontium within the crystallized regions of the glass-ceramic samples. Notably, no detectable boron was observed in any of the analyzed phases, suggesting that B_2O_3 does not incorporate into the crystal lattice and remains within the residual glassy matrix.

The elemental ratios obtained from the EDX analysis closely matched those characteristic of fluorophlogopite, thereby confirming the formation of strontium-substituted fluorophlogopite as the dominant crystalline phase in the heat-treated glass-ceramics. These results provide further evidence of the role of strontium in stabilizing the fluorophlogopite structure and indicate successful phase development through controlled crystallization.

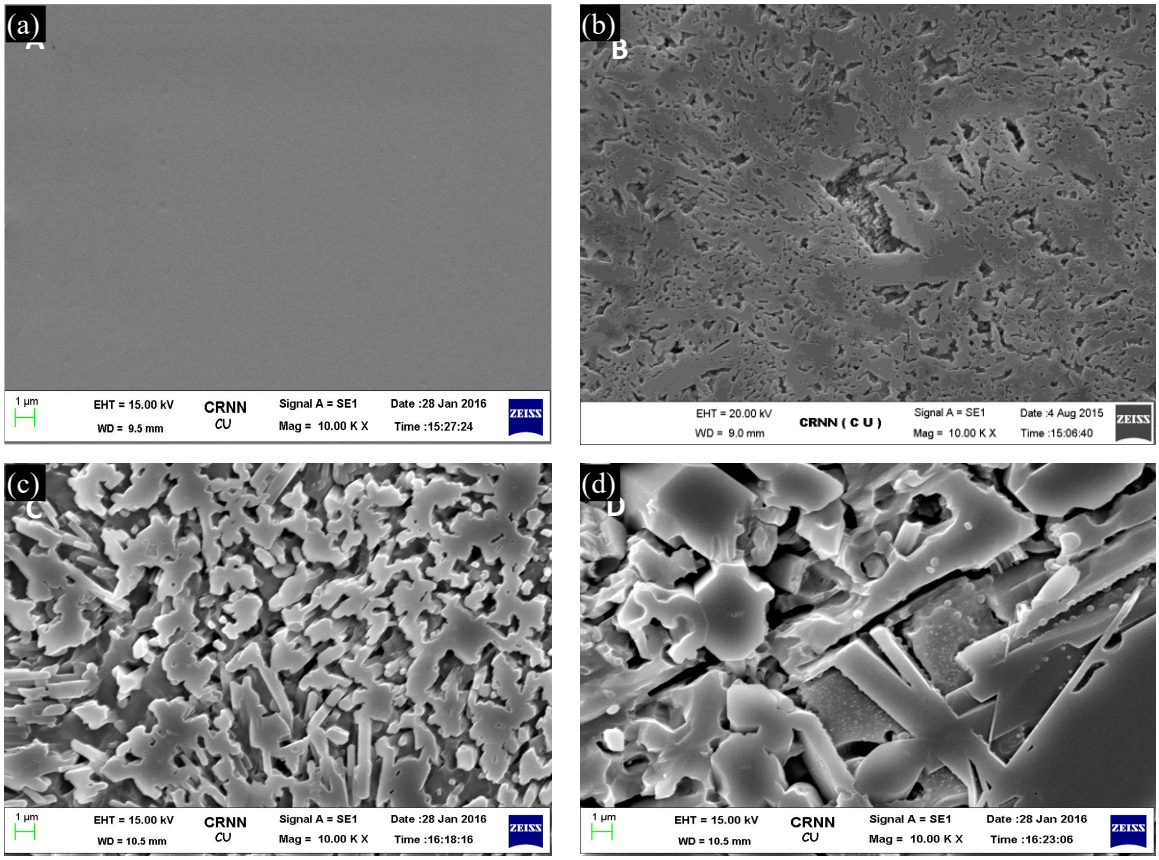

Figure 14. SEM photographs of the polished and etched surface of glass-ceramics sample of B4 ceramized at (a) 800°C, (b) 900°C, (c) 1000°C, (d) 1100°C for 5 h.

Fourier-Transform Infrared Spectroscopy (FT-IR)

Figure 17 presents the FT-IR absorption spectra of the three glass compositions with varying B_2O_3 content. Across all samples, five principal transmittance bands are consistently observed, reflecting the structural features of the glass network. A prominent absorption band near 550 cm^{-1} (denoted as P) corresponds to the bending vibrations of Si–O–Si linkages within SiO_4 tetrahedra. A distinct band around 720 cm^{-1} (Q) is attributed to Al–O vibrations in AlO_4 units, indicating the incorporation of aluminium within the tetrahedral network.

A broad absorption region spanning 846–1199 cm^{-1} (R) is characteristic of overlapping stretching vibrations from Si–O bonds in SiO_4 tetrahedra and B–O bonds in BO_4 units, suggesting the coexistence of both silicon and boron-based glass-forming structures. With increasing B_2O_3 content, particularly in B2 and B6 compositions, an additional sharp peak appears around 1284 cm^{-1} (S), which is ascribed to antisymmetric stretching vibrations of Si–O–Si bonds, indicating enhanced polymerization of the silicate network. Furthermore, samples B4 and B6 exhibit an absorption feature near 1430 cm^{-1} (T), consistent with B–O stretching in BO_3 triangular units, confirming the presence of trigonal borate structures.

These spectral features collectively highlight the evolution of the glass network with increased B_2O_3 addition, emphasizing its role in modifying the structural connectivity and bonding environment within the glass matrix (Table 6).

Density

As illustrated in Figure 18, the density of the glass-ceramic samples initially increases with increasing B_2O_3 content up to a heat-treatment temperature of 900°C. However, a gradual decrease in density is

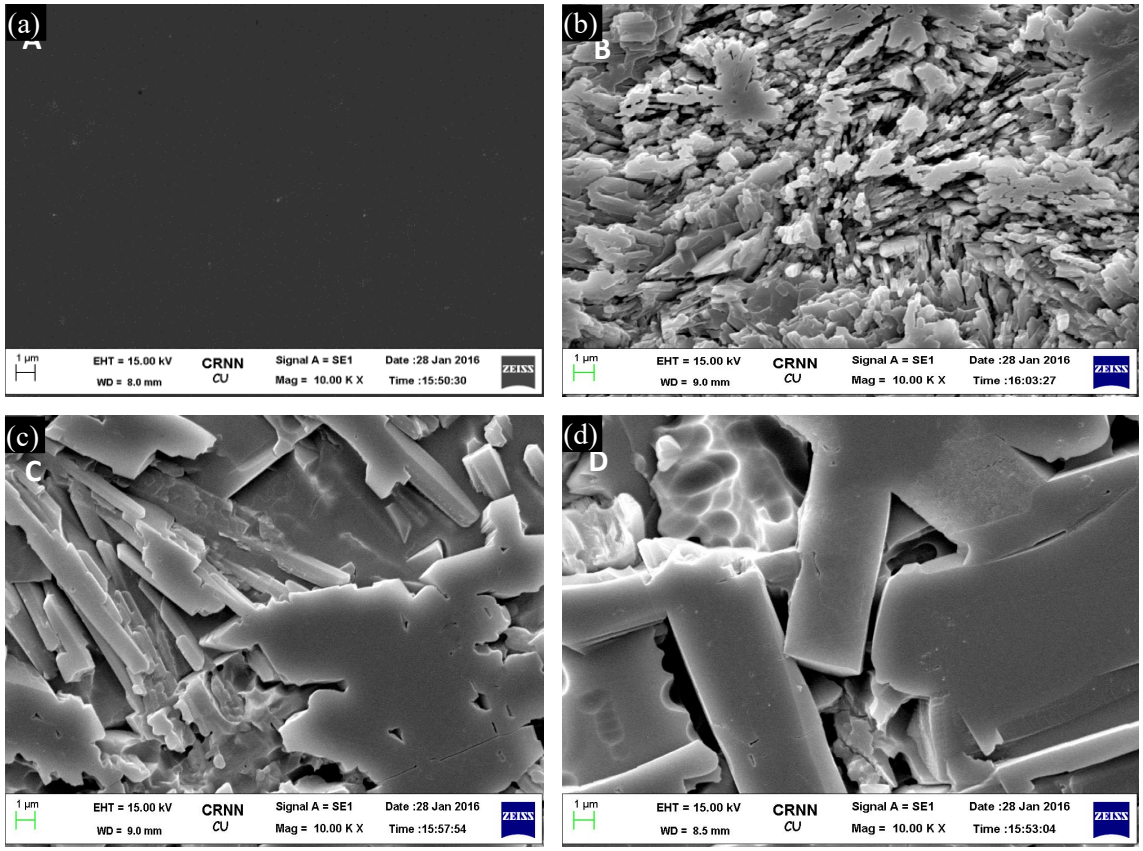

Figure 15. SEM photographs of the polished and etched surface of a glass-ceramics sample of B6 ceramized at (a) 800°C, (b) 900°C, (c) 1000°C, (d) 1100°C for 5 h.

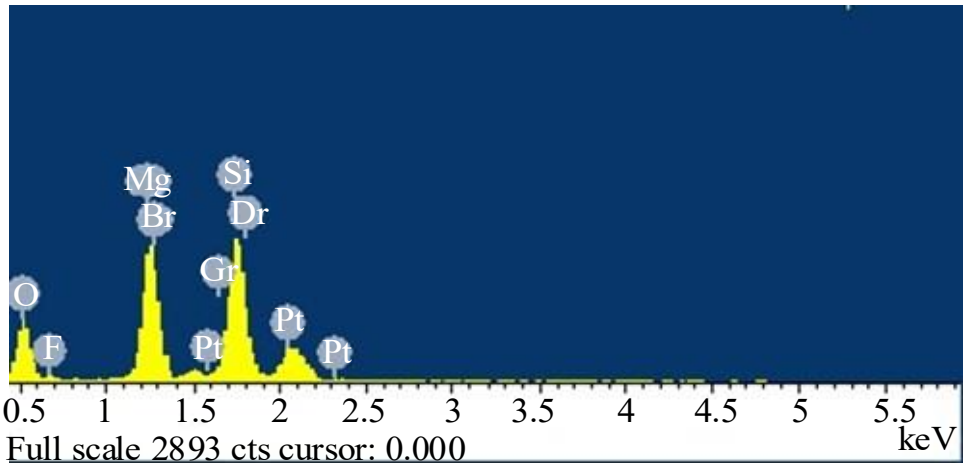

Element	Weight (%)
O	34.22
F	6.55
Mg	13.27
Al	7.35
Si	28.27
Sr	10.34

Figure 16. EDX analysis of the crystal phase of B2 glass batch heat-treated at 1100°C for 5 h.

Table 6. Observed FT-IR spectra in different glass batches.

Glass batch	Wavenumber (cm^{-1})				
	P	***Q***	***R***	***S***	***T***
B2	550	715	846–1199	1284	1430
B4	550	718	846–1156	1284	1430
B6	550	720	846–1151	1284	1430

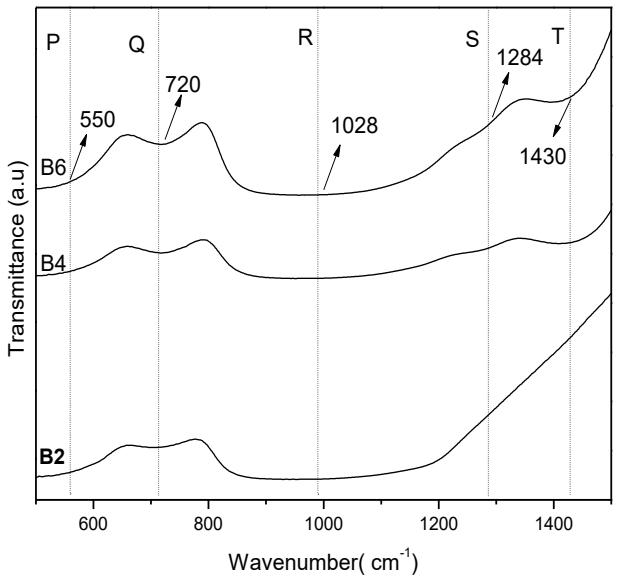

Figure 17. FT-IR spectra of B2, B4, and B6 glass batches.

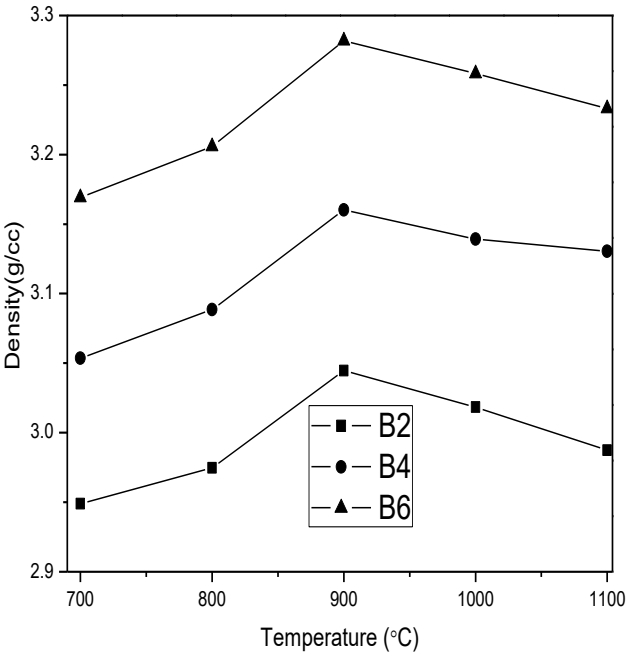

Figure 18. Density of glass and glass-ceramics samples of three batches ceramized at different temperatures for 5 h.

observed at elevated temperatures of 1000 and 1100°C. This reduction in density beyond 900°C can be attributed to the partial decomposition of strontium fluorophlogopite at higher temperatures. Additionally, the formation and propagation of microcracks within the interlocking mica crystals, coupled with crystal growth and a subsequent change in aspect ratio, may further contribute to the observed decline in bulk density.

CONCLUSION

An increase in crystallization peak temperature (Tp) with higher B_2O_3 content leads to a corresponding rise in ΔT (ΔT=Tp−Tg), a critical indicator of glass structural stability. The incorporation of B_2O_3 plays a significant role in modulating the crystallization behavior of mica-based glass-ceramics, enhancing the aspect ratio of crystals, particularly in batches with elevated boron

content. This effect is likely associated with the lower viscosity of the glass matrix at higher B_2O_3 concentrations. The elevated Avrami exponent values (n=2–3.41) observed across all compositions indicate a transition from two-dimensional to three-dimensional crystal growth, suggesting a shift from surface to bulk crystallization mechanisms, especially evident in the B6 batch.

X-ray diffraction analysis confirms the formation of strontium fluorophlogopite as the predominant crystalline phase across all batches, with its abundance increasing up to 1000°C in high-B_2O_3 compositions and subsequently declining at 1100°C, possibly due to partial decomposition at elevated temperatures. This thermal degradation likely contributes to the observed reduction in bulk density. Scanning electron microscopy (SEM) and energy-dispersive X-ray spectroscopy (EDX) further reveal an interlocking crystal morphology embedded within the glass matrix, characteristic of fluorophlogopite. FT-IR spectra support the structural findings, exhibiting absorption bands corresponding to Al–O, B–O, Si–O–Si, and O–Si–O vibrations, indicative of the bonding environment within the boron-modified glass-ceramics.

Acknowledgement
The authors acknowledge the CRNN, University of Calcutta for instrumental support.

Conflict of Interest
All the authors do not have any conflict of interest.

Author Contributions
The manuscript was written with contributions from all authors. All authors have approved the final version of the manuscript.

REFERENCES
1. Aitken B, Beall GH. Glass-ceramics. Mater Sci Technol. 1994; 11: 269–94.
2. Beall GA. In: Hench LL, editors. Adv Nucleation Cryst Glass. Am Ceram Soc; 1972; 251.
3. Machu W. Die physikalischen Eigenschaften des Emails [The physical properties of enamel]. In: Nichtmetallische Anorganische Überzüge [Non-Metallic Inorganic Coatings]. Vienna: Springer; 1952. p. 297-304. doi:10.1007/978-3-7091-5060-3_50. [German].
4. Grossman DG. Machinable glass-ceramics based on tetrasilisic mica. J Am Ceram Soc. 1972; 55(9): 446–9.
5. Radonjic LJ, Nicolic LJ. The effect of fluorine source and concentration on the crystallization of machinable glass-ceramics. J Eur Ceram Soc. 1991; 7(1): 11–6.
6. Beall GH. Mica glass-ceramics. US Patent 3,689,293. 1972.
7. Hoda SN, Beall GH. Alkaline earth mica glass-ceramics. In: Simmons JH, Uhlmann DR, editors. Adv Ceram. 1982; 2: 287–300.
8. Beall GH, Hench LL, Freiman SW. Structure, properties, and nucleation of glass-ceramics. In: Adv. Nucleation Cryst. Glasses. J Am Ceram Soc. 1971; 5: 251–61.
9. Greene K, Pomeroy MJ, Hampshire S, Hill R. Effect of composition on the properties of glasses in the K_2O–BaO–MgO–SiO_2–B_2O_3–MgF_2 system. J Non-Cryst Solids. 2003; 325(1–3): 193–205.
10. James PF. Glass ceramics: new compositions and uses. J Non-Cryst Solids. 1995; 181(1–2): 1–15.
11. James PF. In: Simmson JH, Uhlmann DR, Beall GH, editors. Nucleation and Crystallization in Glasses. Vol. 4. Adv Ceram J Am Ceram Soc; 1982.
12. Honda W, Vogel W, Mortier WJ, Duvigneaud PH, Naessens G, Plumat E. A new type of phlogopite crystal in machinable glass-ceramics. Glass Technol. 1983; 24(6): 318–22.
13. Mallik A, Maiti PK, Kundu P, Basumajumdar A. Influence of B_2O_3 on the crystallization behavior and microstructure of mica glass-ceramics in the system BaO–4MgO–Al_2O_3–6SiO_2–2MgF_2. J Am Ceram Soc. 2012; 95(11): 3505–3508.
14. Hu A-M, Li M, Mao D-L. Crystallization of spodumene-diopside in the LAS glass ceramics with CaO and MgO addition. J Therm Anal Calorim. 2007; 90(1): 185–9.
15. Henry J, Hill RG. Influence of alumina content on the nucleation, crystallization and

microstructure of barium fluorphlogopite glass-ceramics. J Mater Sci. 2004; 39(7): 2499–507.
16. Henry J, Hill RG. The influence of lithia content on the properties of fluorophlogopite glass-ceramics. I. Nucleation and crystallization behavior. J Non-Cryst Solids. 2003; 319(1–2): 1–12.
17. Uno T, Kasuga T, Nakajima K. High strength mica-containing glass-ceramics. J Am Ceram Soc. 1991; 74(12): 3139–41.
18. Uno T, Kasuga T, Nakayam S. Mechanical properties of barium mica-containing glass-ceramics. J Eur Ceram Soc. 1992; 100(1159): 315–9.
19. Uno T, Kasuga T, Nakajima K, Ikushima AJ. Microstructure of Mica-Based Nanocomposite Glass-Ceramics. J Am Ceram Soc. 1993; 76(2): 539–541.
20. Avrami M. Kinetics of phase change. I. General theory. J Chem Phys. 1939; 7(12): 1103–11.
21. Avrami M. Kinetics of phase change. II. Transformation-time relations for random distribution of nuclei. J Chem Phys. 1940; 8(2): 212–4.
22. Avrami M. Kinetics of phase change. III. Granulation, phase change and microstructure. J Chem Phys. 1941; 9(2): 177–84.
23. Kissinger HE. Variation of peak temperature with heating rates in differential thermal analysis. J Res Natl Bur Stand. 1956; 57(4): 217–21.
24. Kissinger HE. Reactions kinetics in differential thermal analysis. Anal Chem. 1957; 29(11): 1702–6.
25. Ozawa T. Temperature control modes in thermal analysis. Pure Appl Chem. 2000; 72(11): 2083–99.
26. Augis JA, Bennett JE. Calculation of the Avrami parameters for heterogeneous solid state reactions using a modification of the Kissinger method. J Therm Anal. 1978; 13: 283–92.
27. Perez-Maqueda LA, Criado JM, Malek J. Combined kinetic analysis for the crystallization kinetics of non-crystalline solids. J Non-Cryst Solids. 2003; 320(1–3): 84–91.
28. Merzbacher CI, White WB. The structure of alkaline earth aluminosilicate glasses as determined by vibrational spectroscopy. J Non-Cryst Solids. 1991; 130(1): 18–34.

